On Nonlinear Flow with Multiple Obstructions

LAWRENCE J. PRATT

Graduate School of Oceanography, University of Rhode Island, Kingston, RI 02882

(Manuscript received 8 June 1983, in final form 28 December 1983)

ABSTRACT

Whereas long-wave theories have proved successful in describing the nonlinear effects of single obstructions on narrow flows, the theories can fail when several obstructions are present. This failure is demonstrated using a simple laboratory flow which is predicted by long-wave theory to be unstable, but which is stabilized in practice by short-wave effects. A nonlinear dispersive theory leads to an interpretation of the short waves as a combination of cnoidal and solitary waves, and upstream control is found for the second (downstream) obstacle only.

1. Introduction

Among the simplest theories of fluid flow which retain full nonlinearity are long-wave theories. The long-wave approximation typically assumes the cross-stream scales of motion to be small compared to the along-stream scale, and often allows the equations of motion to be reduced to a quasilinear set of the form

$$\frac{\partial u_i}{\partial t} + a_{ij}\frac{\partial u_j}{\partial x} = I_i, \tag{1}$$

where a_{ij} is a function of the dependent variables u_i and the along-stream coordinate x. For an inviscid fluid the forcing term I_i is a function of at most u_i and x, and it typically contains the geometric constraints (such as bottom topography) imposed on the flow.

Long-wave theories have been successfully applied to a number of problems involving steady flow over and around obstructions. It is often possible to obtain closed-form steady solutions, as accomplished by Long (1954) for single and multilayer flow over an obstacle; by Whitehead *et al.* (1974) and Gill (1977) for flow through a rotating channel containing an obstacle or side contraction; by Gill and Schumann (1979) and Roed (1980) for a coastal current about a cape or bay; and by numerous other authors in hydraulics and gas dynamics. These investigations typically reveal the existence of a *controlled* solution for which the height or width of the obstruction determines the state far upstream. It will be shown here that the presence of two (or more) such obstructions leads to a situation inadequately described by long-wave theory, and that an appeal to short-wave dynamics must be made in order to obtain a solution. Discussion will be restricted to homogeneous, free-surface flows, although the long-wave failure described will likely occur in any problem which admits a controlled solution.

Consider a steady, homogeneous, inviscid flow with velocity u and depth h which passes over an obstacle of elevation $b(x)$ mounted on a flat bottom of elevation $b(x) = 0$ (Fig. 1a). The long-wave theory for such a flow is based on the assumption that the ratio of the fluid scale-depth H to the horizontal length L of the obstacle is small, i.e., $H/L \ll 1$. The dependent variables in (1) then become

$$u_i = \begin{pmatrix} u \\ h \end{pmatrix}, \quad a_{ij} = \begin{pmatrix} u & g \\ h & u \end{pmatrix}, \quad I = \begin{pmatrix} -gdb/dx \\ 0 \end{pmatrix}, \tag{2}$$

where u is the horizontal velocity, h the fluid depth, g the acceleration due to gravity, and the horizontal velocity u is independent of elevation. If these are substituted into (1), the result can easily be integrated and put into the cubic form

$$(h/h_0)^3 - [1 - (b/h_0) + \mathrm{Fd}^2/2](h/h_0)^2 + \mathrm{Fd}^2/2 = 0, \tag{3}$$

where $\mathrm{Fd} = u_0/(gh_0)^{1/2}$ is a Froude number based on the fluid depth h_0 and velocity u_0 upstream of the obstacle. The general nature of the solution to (3) depends upon Fd and the dimensionless sill height $b1/h_0$ of the obstacle above the flat bottom (Long, 1954). In general, four types of solution are possible, depending upon the signs of Fd and the discriminant

$$D = (b1/h_0) - 1 + \frac{3}{2}\mathrm{Fd}^{2/3} - \frac{1}{2}\mathrm{Fd}^2. \tag{4}$$

An example of each solution is sketched in Fig. 1. Of the four solutions, two have free-surface profiles which are symmetric with respect to the topography, while two are antisymmetric. The two symmetric solutions (Figs. 1a and b) are characterized by $D < 0$, while the antisymmetric solutions (Figs. 1c and d) both have $D = 0$.

Much is revealed about the differences between the solutions in Fig. 1 by their characteristic curves (also

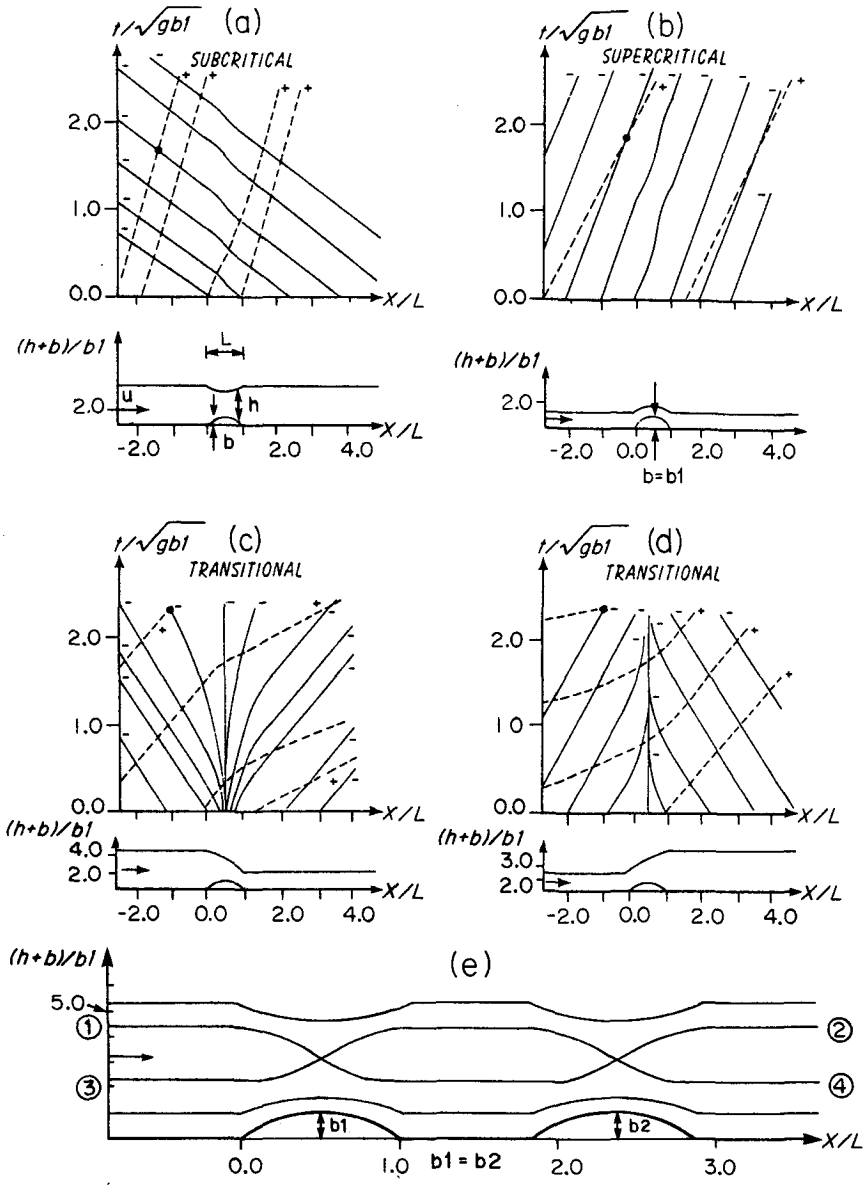

FIG. 1. Examples of the four general solutions to Eq. (3) and the characteristic curves of each. Dashed lines are X_+ characteristics while solid lines are X_- characteristics. The dimensionless flow rate $Q/(g^{1/2}b1^{3/2}) = 3.0$ for each solution. (a) Subcritical, free-surface flow with definition sketch; $b1/h_0 = 0.2$, Fd = 0.37. (b) Supercritical flow: $b1/h_0 = 1.0$, Fd = 4.0. (c) Controlled flow: $b1/h_0 = 0.24$, Fd = 0.45. (d) Unstable transitional flow: $b1/h_0 = 0.42$, Fd = 1.12. (e) Long-wave solutions for flow over two identical obstacles, using above parameters; the obstacles are parabolic in each case.

shown in Figs. 1a–d). These curves determine the positions $X_\pm(t)$ that small amplitude, long gravity-waves would map out propagating with or against the steady flow (as denoted by plus or minus signs). Since the speeds of such waves are $u \pm (gh)^{1/2}$, the characteristic curves are determined by

$$dX_\pm/dt = u \pm (gh)^{1/2}.$$

In all cases $dX_+/dt > 0$, so that the X_+-characteristics tilt downstream, as shown by the dashed lines. However, the first symmetrical solution is characterized everywhere by $dX_-/dt < 0$ (Fig. 1a) while the second symmetrical solution (Fig. 1b) has $dX_-/dt > 0$. In the first case, small disturbances are able to propagate upstream, while in the second case they are not. These solutions are termed "subcritical" and "supercritical," respectively. Both tend to be obtained experimentally when the obstructing obstacle is small in the sense $D < 0$.

The two antisymmetrical solutions are, on the other hand, essentially nonlinear and cannot, for example, be obtained from a theory of infinitesimal topography. Both are transitional with respect to the characteristic speed dX_-/dt. In the first case (Fig. 1c) the flow is subcritical upstream and supercritical downstream of the obstacle's sill. The X_--characteristics thus tilt away from the sill with a single vertical characteristic at the sill. A small disturbance generated over the obstacle will therefore spread upstream and downstream, eventually covering the entire flow field. This is the controlled solution mentioned above. The other transitional solution (Fig. 1d) is supercritical upstream and subcritical downstream of the sill. The X_--characteristics here become asymptotic as $t \to \infty$ to the vertical characteristic at the sill. This solution is unstable to the formation of free-surface shocks since disturbances following X_--characteristics become focused at the sill. When posed as an initial condition, the flow of Fig. 1d will undergo an adjustment which ends with the establishment of the controlled flow in Fig. 1c. None of the laboratory experiments dealing with free-surface flow (e.g., Long, 1954) are able to reproduce the solution of Fig. 1d, nor is this solution commonly mentioned in textbooks and papers on hydraulics.

Suppose now that a second obstacle is placed downstream of the first. If the two obstacles have identical heights, the four possible steady solutions are those sketched in Fig. 1e. Note that both transitional solutions are *no longer entirely stable.* Branch 1–2 (numbers are circled in the figure) is stable over the first obstacle but not the second, while branch 3–4 is stable over the second but not the first. Furthermore, it is not possible to construct a steady, stable solution by piecing together stable segments from 1–2 and 3–4 using hydraulic jumps, for 1–2 and 3–4 contain identical energy levels and a connecting jump would necessarily dissipate energy.[1] One is left with the curious result that no stable, hydraulically controlled solution exists for flow over two obstacles of identical sill elevations.

2. A numerical experiment

To examine the situation predicted above, a numerical integration of the time-dependent long-wave equations (1) and (2) was performed using the initial conditions

$$u(x, 0) = U, \tag{5a}$$

$$h(x, 0) = H, \tag{5b}$$

and the topography

$$\frac{b}{H} = \begin{cases} \frac{1}{10}\left[1 - \frac{1}{4}\cos(5\pi x/3L)\right] & \text{for } \left(0 \leqslant |x/L| < \frac{3}{5}\right) \\ \frac{1}{8}\left[1 - \left(\frac{5}{2}\right)^2\left(|x/L| - \frac{3}{5}\right)^2\right] & \text{for } \left(\frac{3}{5} \leqslant |x/L| \leqslant 1\right) \\ 0 & \text{for } (1 \leqslant |x/L|), \end{cases} \tag{6}$$

where $U/(gH)^{1/2} = 0.6$. Thus, the initial flow is uniform and subcritical and must adjust to a double-silled obstacle. The obstacle is sufficiently high to preclude adjustment to one of the nontransitional solutions, and end boundaries are isolated far enough upstream and downstream of the obstacle to make the x-domain effectively infinite. The solution is computed using a Lax–Wendroff method (Lax and Wendroff, 1960) similar to the scheme employed by Pratt (1983a). The method allows free-surface shocks to arise while insuring that mass and momentum flux continuity is maintained. Such shocks have been found to be important in similar adjustment problems involving single-silled obstacles (e.g., Houghton and Kasahara, 1968).

The numerical solution is shown in Fig. 2. The initial adjustment (Fig. 2a) is similar to the adjustment to a hydraulically controlled state that occurs when a single sill is present (Houghton and Kasahara, 1968). The main feature is a bore which moves upstream and partially blocks the approaching fluid by increasing its depth but decreasing its flow rate. The flow on the downstream face of the obstacle tends toward a supercritical state followed by a hydraulic jump. This situation is only temporarily realized, however, as a new bore forms near the right-hand sill and moves upstream (Figs. 2b and c). This chain of events is repeated periodically and the solution never settles down to a steady state.

Although these results seem to bear out the predictions of steady long-wave theory, numerical integration over a long term leads to a result which is apparently spurious. Each bore that propagates upstream tends to block the upstream flow by decreasing the flow rate and increasing the upstream depth. Eventually, the flow rate is decreased to a fraction of the value that would be obtained if the obstacle had a single sill; a counterintuitive result, to say the least.

Several similar numerical experiments were carried out using obstacles of various shapes and horizontal spacings for the same initial conditions. Although an unsteady state and consequent flow-rate reduction was found in each case, the time scale of the instability (as measured by the elapsed time between successive upstream-propagating bores) was variable. However, no systematic study was made to link this time scale with the geometry of the topography. In view of the labo-

[1] That two connecting solutions must have identical energy levels follows from two facts. First, the volume flow rate $Q = uh$ must be preserved by a stationary hydraulic jump. Second, the characteristic speed $u - (gh)^{1/2}$ must vanish for both solutions at either sill. If these facts are combined, the Bernoulli constant (energy/unit volume) is found to be $B = \frac{3}{2}(gQ)^{2/3} + gb1$, where $b1$ is the elevation of the sills above the flat bottom. Since Q is the same for either solution, B must be preserved.

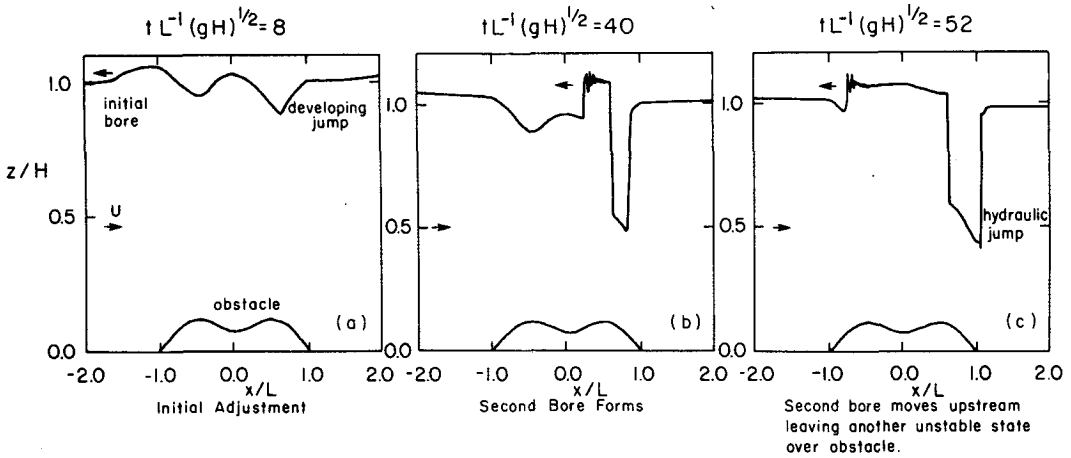

FIG. 2. Numerical results showing long-wave adjustment to the sudden obtrusion of a double-silled obstacle into a uniform flow of velocity U and depth H, with $U/(gH) = 0.6$. Free-surface and obstacle elevations have been nondimensionalized by H, and time by $L(gH)^{-1/2}$, where L is the obstacle length.

ratory results (see below), such a study would be purely academic.

3. A laboratory experiment

The apparent failure of the time-dependent long-wave equations to give a realistic result suggests the need for a laboratory experiment. Such an experiment was performed using the Woods Hole Oceanographic Institution's flume. As shown in Fig. 3, water is circulated through the flume by a variable-speed pump. The fluid enters from the left under a sluice gate, flows through the flume, and spills into a holding tank. In the midsection of the flume two obstacles constructed of flexible sheet metal are attached. The second (downstream) obstacle is fastened at one end to a movable shaft, allowing the obstacle's height $b2$ to be changed. The horizontal spacing between obstacles can also be changed through the use of a movable false bottom, so that a wide variety of topographic settings are possible. The ratio of obstacle height to length is at most 0.08, so that the topography always takes on a long-wave character. The general procedure is to fix the flow rate and obstacle spacing and explore different flow regimes created by varying the relative difference $\Delta b = (b2 - b1)/b1$ in obstacle heights.

The experiments were carried out over a range of upstream Froude numbers ($0.1 < \mathrm{Fd} < 0.8$), relative height differences ($-1.0 > \Delta b > 0.4$), and with horizontal obstacle spacings of zero to five obstacle lengths (although all measurements were made with the obstacles four lengths apart). The most striking finding is that throughout this parameter range the flow is *steady*, despite the predictions of long-wave theory. Fig. 4a contains a sketch of the typical surface profile that is obtained for various values of Fd and obstacle spacings when the obstacles have identical sill heights ($\Delta b = 0$). A photograph of the flow (Plate 1) shows that the fluid surface between the two obstacles looks nothing like that of a long-wave flow. Instead, a regular train of lee waves exists between the two obstacles. Although slight contamination arises from frictional and three-dimensional effects, the most striking departure from long-wave conditions is in the predominantly two-dimensional lee waves. In all experiments the flow upstream of the first obstacle is uniform and subcritical, while that downstream of the second obstacle is uniform and supercritical; the waves exist only

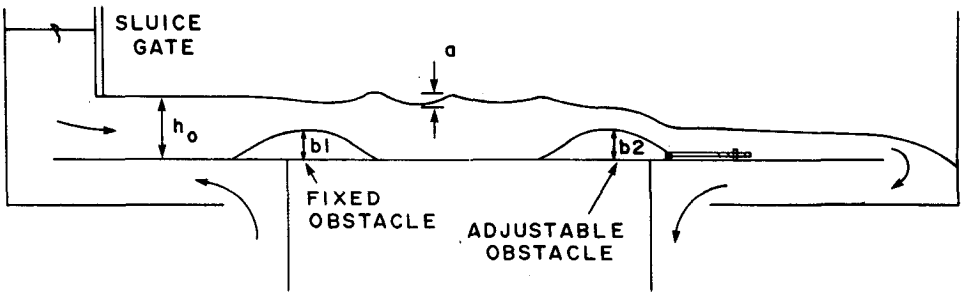

FIG. 3. Cross-section of laboratory flume.

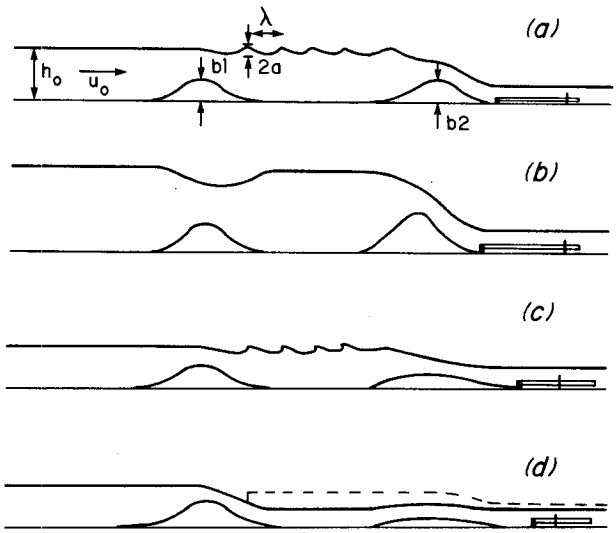

FIG. 4. Sketches of experimentally-found flow regimes. The flow is subcritical upstream of the left-hand obstacle and supercritical downstream of the right-hand obstacle in each case. (a) $b1 \approx b2$; laminar lee-waves between obstacles. (b) $b1 < b2$; long-wave, subcritical flow between obstacles. (c) $b1 > b2$; breaking lee-waves. (d) $b1 \gg b2$; long-wave, supercritical flow between obstacles (solid line) or containing hydraulic jump (dashed line). See text and Fig. 5 for descriptions and parameters.

between the obstacles. Single-obstacle flows with supercritical upstream states are possible (Ippen and Harleman, 1956) but a supercritical upstream flow is difficult to produce with the Woods Hole equipment.

The parametric extent of the flow regime described above is mapped out in Fig. 5 in terms of Δb and Fd for the case in which the obstacles are spaced four lengths apart. The region in which the previously-described lee waves occur is delineated by the solid lines. Other flow regimes exist to the right and left. For example, if the height of the second obstacle is increased over that of the first, causing Δb to become increasingly positive, the amplitudes of the lee waves gradually decrease and the free surface eventually takes on the long-wave appearance sketched in Fig. 4b. This regime occupies the right-hand side of Fig. 5. Lowering the height of the second obstacle below that of the first causes the lee waves to break, as sketched in Fig. 4c and represented by the left-hand portion of Fig. 5. If the second obstacle is lowered further, one of two possible long-wave states is eventually established. The first (indicated by the solid profile in Fig. 4d) contains a supercritical flow at all points downstream of the first obstacle, while the second (dashed profile in Fig. 4d) contains a hydraulic jump in the lee of the first obstacle. Instances can be found in which each of the two states occur for the same values of Δb and Fd. Which of the two possibilities is realized in a given experiment depends on the manner in which Δb and Fd are set. For example, the flow containing the jump can be established by decreasing Δb from a value of zero to a fixed value $(\Delta b)_0 < 0$, whereas the jump may vanish if Δb is further decreased and then raised back to $(\Delta b)_0$. This behavior is not surprising in view of similar types of hysteresis found by Pratt (1983a) in connection with single-obstacle single-layer flows, and by P. G. Baines (personal communication, 1983) in

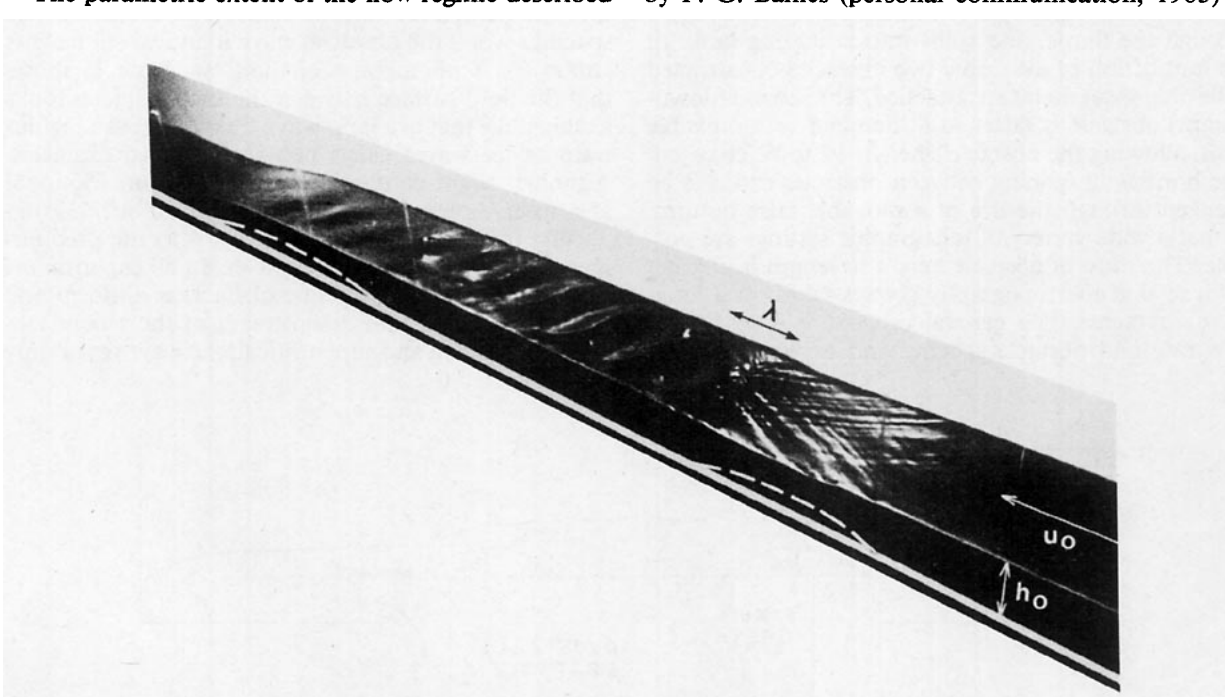

PLATE 1. Photograph of experimental flow for the case $\Delta b = 0$ and Fd = 0.41. The obstacles are outlined in white.

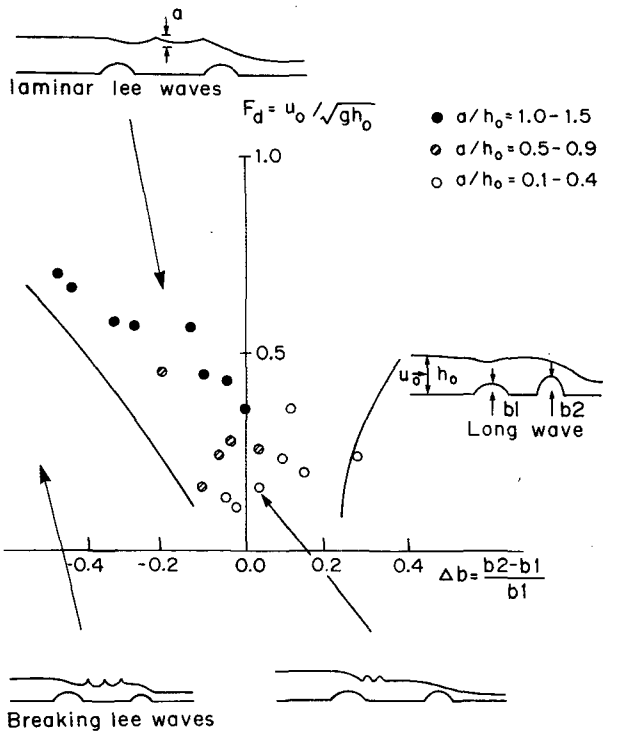

FIG. 5. Experimental results showing different flow regimes as function of $\Delta b = (b2 - b1)/b1$, and Froude number $Fd = u_0/(gh_0)^{1/2}$ measured upstream of first obstacle. The relative amplitude a/h_0 of the laminar wave nearest the upstream obstacle is indicated by the type of dot, as defined in the figure.

connection with single obstacle, two-layer flows. However, determination of the boundary between the breaking lee-wave and long-wave regimes is understandably difficult, and has not been made here. In any case, the boundary will lie to the left of the boundary between laminar and breaking lee waves in Fig. 5.

Within the region of laminar lee waves there are considerable variations in wavelength and amplitude. The approximate length λ and amplitude a of the lee wave nearest the first (upstream) obstacle are indicated in Figs. 5 and 6, respectively. For small values of Fd, the lee waves tend to have small lengths and amplitudes and are concentrated near the upstream obstacle in the manner of an undular jump (Figs. 5 and 6). As Fd increases, the lee waves lengthen and grow in relative amplitude while taking on narrow crests and broad troughs. For values of $Fd > 0.8$, λ becomes greater than the distance between the two obstacles, preventing measurement of λ and a.

While the general character of the laboratory flow is sensitive to Δb and Fd, it is generally insensitive to the spacing between obstacles, particularly within the laminar lee wave region. Increasing the distance between obstacles merely increases the *number* of lee waves without changing the lengths or amplitudes of the existing waves. Also, experiments with other obstacle shapes, including the shape used in the numerical experiment (Fig. 2), were carried out. In each case, steady flows of the previously-described character are produced. Only the details of the wave amplitudes and lengths are found to depend on obstacle shape. No attempt was made to quantify this relationship.

One further result, which will enter prominently in the theory to be described below, is that the obstacle heights are reduced to zero as the upstream Froude number Fd approaches unity. This information does not appear in Figs. 5 or 6, but it is consistent with long-wave theory in the sense that $b1/h_0 \rightarrow 0$ as $Fd \rightarrow 1$ in Eq. (4) with $D = 0$.

To summarize, the unsteady behavior predicted by long-wave theory fails to appear in any laboratory case. Furthermore, the long-wave equations fail to predict the free-surface profile between the two obstacles over a considerable range in values of Δb. For example, laminar lee waves exist at $Fd = 0.4$ for values of Δb as large as 0.3 and as small as -0.35, as shown in Fig. 5. (The theoretical discussion in Section 1 concerning the stability of the long-wave solutions was restricted to $\Delta b = 0$.)

4. Theory

I now seek a more quantitative dynamical explanation for the experimental results described above. Although a theory covering the entire parameter range of Fig. 5 would be intractable, some progress can be

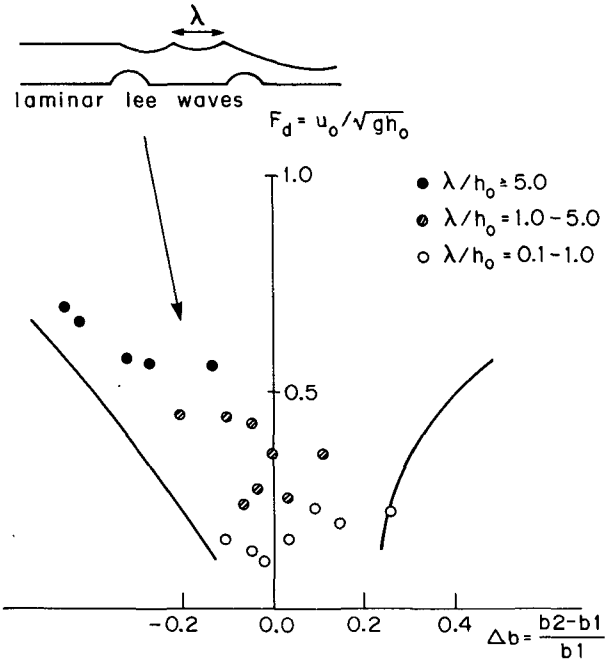

FIG. 6. As in Fig. 5, but showing measurements of the length λ of the laminar lee-wave nearest the upstream obstacle, as represented by the type of dot as defined in the figure.

made if attention is restricted to the upper portion of the diagram (approximately $0.6 < \mathrm{Fd} < 1.0$). In this parameter range the upstream flow is slightly subcritical, the lee waves tend to be nonbreaking, and the typical lee-wave length is large in comparison with the depth. Thus, the vertical aspect ratio δ ($=\lambda/h_0$), based on the upstream depth, tends to be moderately small. A further parameter restriction results from the experimental finding, mentioned earlier, that the obstacle heights are small in comparison to h_0 for values of Fd near unity.

The wave-like flow observed in the laboratory experiment will be explained in terms of inviscid processes. Viscosity is thought to be unimportant in that the viscous boundary layer thickness along the bottom and side walls of the flume are several orders of magnitude less than the depth and width of the flow. Only in the case of breaking waves or very short laminar waves (as occur for small values of Fd in Fig. 6) should viscosity be important.

The inviscid two-dimensional equations of motion and mass conservation describing the steady flow are

$$uu_x + wu_z = -p_x/\rho, \tag{7a}$$

$$uw_x + ww_z = -p_z/\rho - g, \tag{7b}$$

$$u_x + w_z = 0, \tag{7c}$$

where w is the vertical velocity of the fluid, ρ the (constant) density, p the pressure, and z is the vertical coordinate. Other variables retain the meanings assigned earlier, although it should be noted that the horizontal velocity u is no longer necessarily independent of z.

The flow is also assumed to be irrotational:

$$u_z - w_x = 0. \tag{7d}$$

At the free surface, where $z = h + b$, the pressure is taken as zero:

$$p = 0, \quad \text{at} \quad z = h + b, \tag{7e}$$

while the surface and bottom kinematic conditions are

$$w = ud(h + b)/dx, \quad \text{at} \quad z = h + b, \tag{7f}$$

$$w = db/dx, \quad \text{at} \quad z = b. \tag{7g}$$

If λ and h_0 are chosen as horizontal and vertical length scales, $(gh_0)^{1/2}$ and $g^{1/2}h_0^{3/2}/\lambda$ as horizontal and vertical velocity scales, and ρgh_0 as a pressure scale, the following dimensionless variables can be defined:

$$x' = x/\lambda, \qquad z' = z/h_0,$$

$$u' = u/(gh_0)^{1/2}, \quad w' = w\lambda/g^{1/2}h_0^{2/3},$$

$$p' = p/\rho gh_0, \qquad b' = b/h_0.$$

Substitution of these new variables into (7a–g) results, upon dropping primes, in the dimensionless set

$$uu_x + wu_z = -p_x, \tag{8a}$$

$$\delta^2(uw_x + ww_z) = -p_z - 1, \tag{8b}$$

$$u_x + w_z = 0, \tag{8c}$$

$$u_z - \delta^2 w_x = 0, \tag{8d}$$

$$p = 0, \quad \text{at} \quad z = h + b, \tag{8e}$$

$$w = ud(h + b)/dx, \quad \text{at} \quad z = h + b, \tag{8f}$$

$$w = udb/dx, \quad \text{at} \quad z = b. \tag{8g}$$

The experimentally observed smallness of the vertical aspect ratio $\delta = h_0/\lambda$ for $0.6 < \mathrm{Fd} < 1.0$ suggests an expansion of the dependent variables in powers of δ^2. Thus, we write

$$u = u^{(0)} + \delta^2 u^{(1)} + \delta^4 u^{(2)} + \cdots, \tag{9a}$$

$$w = w^{(0)} + \delta^2 w^{(1)} + \delta^4 w^{(2)} + \cdots, \tag{9b}$$

$$p = p^{(0)} + \delta^2 p^{(1)} + \delta^4 p^{(2)} + \cdots, \tag{9c}$$

$$h = h^{(0)} + \delta^2 \eta^{(1)} + \delta^4 \eta^{(2)} + \cdots, \tag{9d}$$

$$b = \delta^2 b^{(1)} + \delta^4 b^{(2)} + \cdots. \tag{9e}$$

The assumption $b^{(0)} = 0$ is based on the previously noted observation of obstacle smallness.

If (9a–e) are substituted into (8a–g), the result, to lowest order, is

$$u^{(0)}u_x^{(0)} + w^{(0)}u_z^{(0)} = -p_x^{(0)}, \tag{10a}$$

$$0 = -p_z^{(0)} - 1, \tag{10b}$$

$$u_x^{(0)} + w_z^{(0)} = 0, \tag{10c}$$

$$u_z^{(0)} = 0, \tag{10d}$$

$$p^{(0)} = 0, \quad \text{at} \quad z = h^{(0)}, \tag{10e}$$

$$w^{(0)} = u^{(0)}dh^{(0)}/dx, \quad \text{at} \quad z = h^{(0)}, \tag{10f}$$

$$w^{(0)} = 0, \quad \text{at} \quad z = 0. \tag{10g}$$

It is immediately evident that the horizontal pressure gradient and velocity are independent of elevation. If (10b) is integrated with respect to z and (10e) applied, the O(0) pressure is found to be

$$p^{(0)} = h^{(0)} - z.$$

If this pressure is substituted into (10a), and (10d) is applied, the resulting momentum equation is

$$u^{(0)}du^{(0)}/dx + dh^{(0)}/dx = 0. \tag{11}$$

Similarly, (10c) can be integrated from $z = 0$ to $z = h^{(0)}$ and the boundary conditions (10f, g) applied, resulting in

$$h^{(0)}du^{(0)}/dx + u^{(0)}dh^{(0)}/dx = 0. \tag{12}$$

This equation along with (11) comprises the homogeneous version of the long-wave theory (1) and (2).

Since topographic forcing is absent, the only solutions are uniform flows:

$$u^{(0)} = \text{constant}, \tag{13a}$$

$$h^{(0)} = \text{constant}, \tag{13b}$$

$$w^{(0)} = 0. \tag{13c}$$

To $O(\delta^2)$, Eqs. (8a–g) become

$$u^{(0)}u_x^{(1)} = -p_x^{(1)}, \tag{14a}$$

$$0 = -p_z^{(1)}, \tag{14b}$$

$$u_x^{(1)} + w_z^{(1)} = 0, \tag{14c}$$

$$u_z^{(1)} = 0, \tag{14d}$$

$$p^{(1)} - (\eta^{(1)} + b^{(1)}) = 0, \quad \text{at} \quad z = h^{(0)}, \tag{14e}$$

$$w^{(1)} = u^{(0)}d(\eta^{(1)} + b^{(1)})/dx, \quad \text{at} \quad z = h^{(0)}, \tag{14f}$$

$$w^{(1)} = u^{(0)}db^{(1)}/dx, \quad \text{at} \quad z = 0, \tag{14g}$$

where (10b) and each of equation of (13) have been used to simplify various terms. Also, the boundary conditions (14e–g) have been applied at the elevations $z = h$ and $z = b$ through the usual Taylor expansions about $z = h^{(0)}$ and $z = 0$.

The $O(\delta^2)$ fields continue to be of long-wave character, as evidenced by the independence of $u^{(1)}$ and $p_z^{(1)}$ on elevation z. Proceeding as before, (14b) can be integrated with respect to z, (14e) applied, and the result substituted into (14a) to form the momentum equation

$$u^{(0)}du^{(1)}/dx + d\eta^{(1)}/dx = -db^{(1)}/dx. \tag{15}$$

Integrating (14c) from $z = 0$ to $z = h^{(0)}$ and applying (14f) and (14g) gives

$$h^{(0)}du^{(1)}/dx + u^{(0)}d\eta^{(1)}/dx = 0. \tag{16}$$

Equations (15) and (16) can be combined to form a single expression for $\eta^{(1)}$:

$$d\eta^{(1)}/dx = (u^{(0)2} - h^{(0)})^{-1}h^{(0)}db^{(1)}/dx. \tag{17}$$

The structure of $\eta^{(1)}$ in (17) depends on the value of $u^{(0)2} - h^{(0)}$. If $u^{(0)2} - h^{(0)} \neq 0$, $\eta^{(1)}$ is simply proportional to $b^{(1)}$ and no wave-like behavior independent of the topography is possible. If, on the other hand, $u^{(0)2} = h^{(0)}$, the situation is more complex. First of all, the $O(\delta^2)$ topography $b^{(1)}$ must vanish to prevent $d\eta^{(1)}/dx$ from becoming unbounded. In this case (15) and (16) are redundant and $\eta^{(1)}$ is indeterminate. The interpretation of this behavior is clear: Long-wave disturbances propagating against the O(0) flow move at dimensionless speed $u^{(0)} - h^{(0)1/2}$. In order for steady disturbances to exist independent of topography, this speed must be zero; $u^{(0)} = h^{(0)1/2}$. However, this critical condition causes the $O(\delta^2)$ dynamics [i.e., Eqs. (15) and (16)] to become degenerate and the structure of $\eta_{(x)}^{(1)}$ (and $u_{(x)}^{(1)}$) becomes sensitive to the delicate balance of forces and accelerations at $O(\delta^4)$. This behavior is not unlike the "critical level" phenomenon (Booker and Bretherton, 1967) often encountered in connection with internal gravity waves in shear flows. [It must be cautioned that the degenerate behavior of the *linear* equations (15) and (16) is not a feature of the *nonlinear* equations (11) and (12). Solutions to the former are arbitrary functions of x for $u^{(0)2} - h^{(0)} = 0$, while solutions to the latter are constants regardless of the value of $u^{(0)2} - h^{(0)}$.]

Since the present analysis is designed for flows with upstream Froude numbers near unity, it is now formally assumed that the O(0) uniform flow be critical:

$$u^{(0)2} = h^{(0)}. \tag{18}$$

(This formally restricts discussion to the upper portions of Figs. 5 and 6). Equation (17) then demands that

$$b^{(1)} = 0. \tag{19}$$

The only information now given by (15) and (16) is the following relationship between $u^{(1)}$ and $\eta^{(1)}$:

$$h^{(0)}u^{(1)} = -u^{(0)}\eta^{(1)} + u^{(0)}\Delta, \tag{20}$$

obtained by integrating (16) and using (18). The integration constant Δ determines an $O(\delta^2)$ correction to the basic flow rate $u^{(0)}h^{(0)}$. Also, the $O(\delta^2)$ vertical velocity, obtained by integrating (14c) and applying (14g) to the result is

$$w^{(1)} = -zdu^{(1)}/dx. \tag{21}$$

To $O(\delta^4)$, Eqs. (8a–g) are

$$u^{(0)}u_x^{(2)} + p_x^{(2)} = -u^{(1)}u_x^{(1)}, \tag{22a}$$

$$u^{(0)}w_x^{(1)} = -p_z^{(2)}, \tag{22b}$$

$$u_x^{(2)} + w_z^{(2)} = 0, \tag{22c}$$

$$u_z^{(2)} - w_x^{(1)} = 0, \tag{22d}$$

$$p^{(2)} = \eta^{(2)} + b^{(2)}, \quad \text{at} \quad z = h^{(0)}, \tag{22e}$$

$$w^{(2)} = u^{(0)}d(\eta^{(2)} + b^{(2)})/dx + d(u^{(1)}\eta^{(1)})/dx, \quad \text{at} \quad z = h^{(0)}, \tag{22f}$$

$$w^{(2)} = u^{(0)}db^{(2)}/dx, \quad \text{at} \quad z = 0. \tag{22g}$$

If (21) is used to substitute for $w^{(1)}$ in (22b), the result integrated with respect to z, and the boundary condition (22e) applied, the $O(\delta^4)$ pressure is found to be

$$p^{(2)}(x, z) = \eta^{(2)} + b^{(2)} + \frac{1}{2}u^{(0)}(z^2 - h^{(0)2})d^2u^{(1)}/dx^2. \tag{23}$$

The pressure is no longer hydrostatic, a crucial departure from the lower-order dynamics.

The $O(\delta^4)$ horizontal velocity can be obtained by using (21) to substitute for $w^{(1)}$ in (22d) and integrating with respect to z. The result is

$$u^{(2)}(x, z) = u^{(2)}(x, h^{(0)}) + \frac{1}{2}(h_0^2 - z^2)d^2u^{(1)}/dx^2. \quad (24)$$

Note that the horizontal velocity is no longer z-independent. If the above expression for $u^{(2)}$ is now substituted into (22c), the result integrated from $z = 0$ to $z = h^{(0)}$, and the boundary conditions (22f, g) applied, the free-surface horizontal velocity $u^{(2)}(x, h^{(0)})$ is found to be given by

$$\frac{du^{(2)}(x, h^{(0)})}{dx} = -\frac{1}{3}h^{(0)2}\frac{d^3u^{(1)}}{dx^3} - h^{(0)-1}\left[u^{(0)}\frac{d\eta^{(2)}}{dx} + \frac{d(u^{(1)}\eta^{(1)})}{dx}\right]. \quad (25)$$

The horizontal momentum balance (22a) can now be evaluated by substituting the above expressions for $u^{(2)}(x, z)$ and $p^{(2)}(x, z)$ and writing $u^{(1)}(x)$ in terms of $\eta^{(1)}(x)$ with the aid of (20). If this is done, the result is

$$\left(1 - \frac{u^{(0)2}}{h^{(0)}}\right)h^{(0)-2}\frac{d\eta^{(2)}}{dx} = -\frac{1}{3}\left(\frac{u^{(0)2}}{h^{(0)}}\right)\frac{d^3\eta^{(1)}}{dx^3} + 2\left(\frac{u^{(0)2}}{h^{(0)}}\right)^2\left(\Delta - \frac{3}{2}\eta^{(1)}\right)\frac{d\eta^{(1)}}{dx} - h^{(0)-2}\frac{db^{(2)}}{dx}.$$

Since $u^{(0)2} = h^{(0)}$, the right-hand side of the above equation must vanish, leaving

$$d^3\eta^{(1)}/dx^3 = 6\left(\Delta - \frac{3}{2}\eta^{(1)}\right)d\eta^{(1)}/dx - 3d\tilde{b}^{(2)}/dx, \quad (26)$$

where $\tilde{b}^{(2)} = h^{(0)2}b^{(2)}$. A single integration with respect to x yields

$$d^2\eta^{(1)}/dx^2 = \frac{9}{2}\left(\frac{4}{3}\Delta - \eta^{(1)}\right)\eta^{(1)} - 3\tilde{b}^{(2)} + B^{(1)}. \quad (27)$$

Since (26) is a momentum equation, its integral (27) can be interpreted as an energy equation with the integration constant $B^{(1)}$ representing the Bernoulli constant. If one removes the dispersive term $d^2\eta^{(1)}/dx^2$ from (27), the result is a simple quadratic equation, the solutions of which behave in a similar way to the long-wave solutions of Fig. 1. The dispersive term owes its existence to the nonhydrostatic effects which arise at $O(\delta^4)$.

The homogeneous form of Eq. (26) has also been derived by Keller (1948) and Benjamin and Lighthill (1954) in connection with studies of stationary waves in steady flows over a flat bottom. The basic approach used here is similar to Keller's, although the notation and ordering of terms in his derivation are somewhat different.

5. Cnoidal and solitary waves and nonhomogeneous solutions

Closed-form solutions to (27) are difficult to obtain unless the bottom topography $\tilde{b}^{(2)}_{(x)}$ is trivial or assumes a special form. However, some insight into the behavior of solutions for general topography can be gained by introducing the free surface slope $Y^{(1)} = d\eta^{(1)}/dx$ as a dependent variable, so that (27) becomes

$$dY^{(1)}/dx = \frac{9}{2}\left(\frac{4}{3}\Delta - \eta^{(1)}\right)\eta^{(1)} - 3\tilde{b}^{(2)} + B^{(1)}, \quad (28)$$

$$d\eta^{(1)}/dx = Y^{(1)}. \quad (29)$$

The behavior of (28) and (29) can be discussed using the phase plane (Poincaré diagram) in which solutions are mapped out in terms of the dependent variables $\eta^{(1)}$ and $Y^{(1)}$, with the independent variable x appearing as a parameter determining position along each phase curve. However, since $\tilde{b}^{(2)}$ is a predetermined function of x, (28) and (29) are nonautonomous and the shapes of the phase curves vary with x over nonflat sections of the bottom. To momentarily avoid this complication, it will temporarily be assumed that $\tilde{b}^{(2)}$ is constant, so that the bottom is flat.

First consider the equilibrium points of (28) and (29), for which $dY^{(1)}/dx = d\eta^{(1)}/dx = 0$, and which therefore correspond to uniform flows. The locations of such points are given by

$$\left.\begin{aligned} Y^{(1)} &= 0 \\ \eta^{(1)}_{\pm} &= \frac{2}{3}\left[\Delta \pm \left(\Delta^2 - \frac{3}{2}\tilde{b}^{(2)} + \frac{1}{2}B^{(1)}\right)^{1/2}\right] \end{aligned}\right\}. \quad (30)$$

Two real and distinct equilibrium points exist for

$$\Delta^2 > \frac{3}{2}\tilde{b}^{(2)} - \frac{1}{2}B^{(1)}, \quad (31)$$

and these points coalesce when

$$\Delta^2 = \frac{3}{2}\tilde{b}^{(2)} - \frac{1}{2}B^{(1)}. \quad (32)$$

In the latter case, the $O(\delta^2)$ surface displacement is given by (30) as

$$\eta^{(1)}_{\pm} = \eta^{(1)}_e = \frac{2}{3}\Delta. \quad (33)$$

Now consider the Froude number for the uniform flows described above:

$$\begin{aligned} \mathrm{Fd} &= (u^{(0)} + \delta^2u^{(1)})(h^{(0)} + \delta^2\eta^{(1)})^{-1/2} \\ &= u^{(0)}/h^{(0)1/2} + \delta^2u^{(0)}\left(\Delta - \frac{3}{2}\eta^{(1)}\right)\Big/h^{(0)3/2} + O(\delta^4) \\ &\approx 1 + \delta^2h^{(0)-1}\left(\Delta - \frac{3}{2}\eta^{(1)}\right), \end{aligned} \quad (34)$$

where (18) and (20) have been used in the final step. If (32) and (33) hold, so that a single uniform value of $\eta^{(1)}$ exists, then the $O(\delta^2)$ term in (34) vanishes. In this case the criticality of the flow is preserved at $O(\delta^2)$. If, on the other hand, (31) holds, there exist two distinct uniform values $\eta^{(1)}_+$ and $\eta^{(1)}_-$ such that

$$\eta^{(1)}_+ > \frac{2}{3}\Delta, \quad \eta^{(1)}_- < \frac{2}{3}\Delta,$$

corresponding to *slightly subcritical* and *slightly supercritical* uniform flows, in view of (34). A bifurcation thus occurs at the point $\eta_{\pm}^{(1)} = \frac{2}{3}\Delta$; the uniform critical flow being split into subcritical and supercritical parts.

Figure 7 contains two phase planes; one corresponding to $\tilde{b}^{(2)} = 0$, the other to $\tilde{b}^{(2)} = 0.5$, and both with $B^{(1)} = 0$ and $\Delta = -1$. First consider the $\tilde{b}^{(2)} = 0$ plane (Fig. 7a). Since (31) is satisfied, two uniform flows exist, and these appear on the $\eta^{(1)}$ axis as $\eta_{+}^{(1)} = 0$ and $\eta_{-}^{(1)} = -\frac{4}{3}$. The former is a stable *center point* corresponding to a slightly subcritical flow and is surrounded by closed phase trajectories. These trajectories represent periodic cnoidal waves (Keller, 1948) containing broad troughs and narrow crests, as evidenced by the asymmetry of the trajectories with respect to $\eta^{(1)}$. Bounding the cnoidal waves is a phase trajectory representing a wave with a single crest, and troughs which merge into the uniform flow at $(-4/3, 0)$. This trajectory represents a solitary wave, and the point $(-4/3, 0)$ a uniform, slightly supercritical flow. Outside the solitary wave the phase trajectories extend infinitely far from the equilibrium points, indicating a lack of boundedness in the corresponding solutions.

The effect of increasing the bottom elevation to $\tilde{b}^{(2)} = 0.5$ is shown in Fig. 7b. The uniform flows now appear at $\eta_{+}^{(1)} = -0.33$ and $\eta_{-}^{(1)} = -1.0$, and the envelope of bounded solutions has been shrunk.

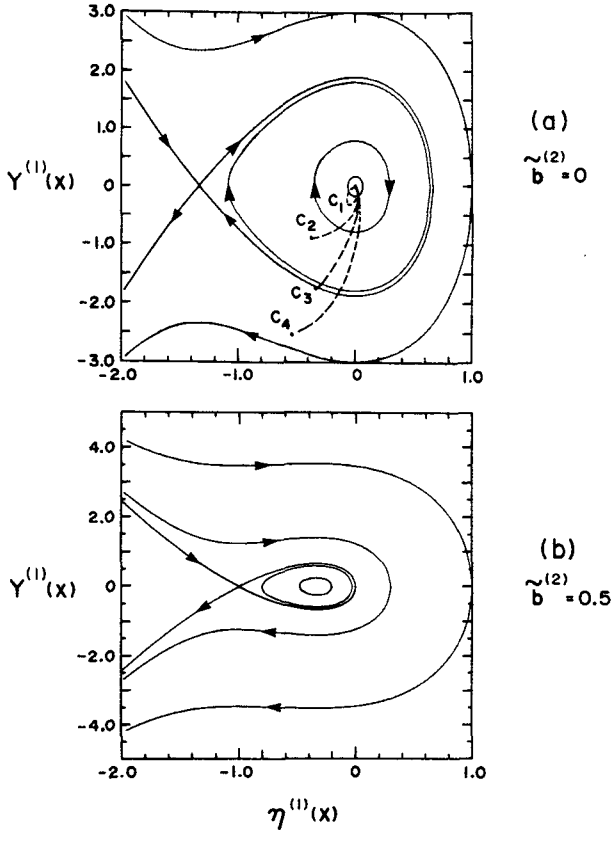

FIG. 7. Phase plane diagrams for Eqs. (28) and (29), with constant $\tilde{b}^{(2)}$ and $\Delta = -1.0$. (a) $\tilde{b}^{(2)} = 0$; (b) $\tilde{b}^{(2)} = 0.5$.

Now suppose that the bottom is no longer flat but contains two obstacles of the same general configuration used in the laboratory experiment. The flat portions of the bottom are assumed to have zero elevation, so that the solutions of Fig. 7a are valid there. If the upstream flow is uniform and slightly subcritical, as in the experiments, then the upstream solution lies at the origin. Consider the behavior of the solution curve over the first obstacle. As the fluid moves up the face of the first obstacle, $\tilde{b}^{(2)}$ increases and the center point is drawn to the left. The initial tendency of the actual solution curve, however, is to remain at the origin (since $d\eta^{(1)}/dx$ is initially zero). As closed trajectories are swept past the origin, the solution curve takes on a phase velocity tangent to the passing trajectories as indicated by the dashed lines in Fig. 7a. As the first obstacle is passed the trajectories expand back to their original shapes, but the net effect is to place the solution curve on a trajectory away, in general, from the center point. There are four possibilities in all, as indicated in Fig. 7a. The first (labeled C_1) places the downstream solution back at the center point, implying a uniform, slightly subcritical flow downstream of the first obstacle (also see Fig. 8a). In this case, the upstream and downstream states are identical. The second (labeled C_2) connects the center point with one of the periodic trajectories. In this case the flow downstream of the first obstacle contains lee waves. The third possibility (labeled C_3) places the downstream solution on the limiting trajectory corresponding to the solitary wave. In this case the solution approaches a uniform, slightly supercritical state downstream of the first obstacle. The final possibility (labeled C_4) joins the center point to one of the open trajectories outside the solitary wave, leading to an unbounded state. Examples of the three bounded solutions have been computed numerically and appear in Figs. 8a–c. Of these three possible bounded solutions, it is interesting that two (Figs. 8a and c) resemble the long-wave solutions shown in Figs. 1a and c, while the third (Fig. 8b) is completely new.

If a second obstacle appears in the channel, the number of possible steady configurations is again increased threefold. (For n obstacles there are 3^n possible steady configurations.) Of the nine possible bounded, steady configurations, the one selected in the laboratory experiment contains cnoidal waves downstream of the first obstacle, and the partial solitary wave downstream of the second (see Fig. 8d). This raises several questions. First, why should the partial solitary wave occur at all, as the phase plane seems to indicate that the solitary wave is a rather special solution? Second, why should the partial solitary wave occur always downstream of the second obstacle and never the first? Finally, what determines the values of $B^{(1)}$ and Δ in a given experiment?

Recall that one outcome among the possible solution curves in Fig. 7a is an unbounded downstream state. This behavior would indicate that the upstream conditions are improperly specified. Under such conditions

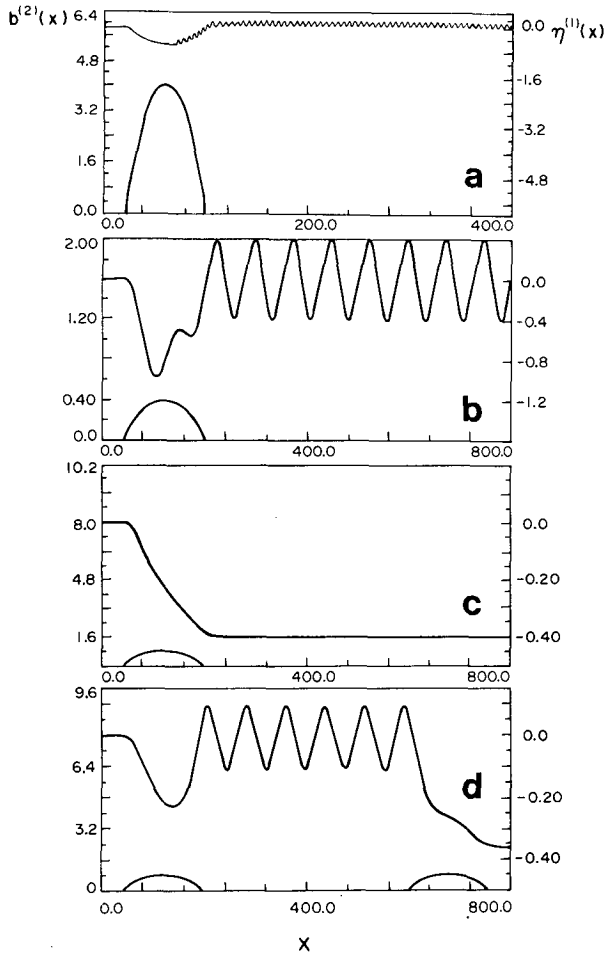

FIG. 8. Numerical solutions to (28) and (29) for the topography:

$$\tilde{b}^{(2)} = \begin{cases} 0 & (|x - 30| > 1) \\ \tilde{b}^{(2)}_{\max}\{1 - [(x/30) - 2]^2\} & (|x - 30| \leq 1) \end{cases}$$

in (a), and

$$\tilde{b}^{(2)} = \begin{cases} 0 & (|x - 60| > 1) \\ \tilde{b}^{(2)}_{\max}\{1 - [(x/60) - 2]^2\} & (|x - 60| \leq 1) \end{cases}$$

in (b), (c), and (d). The upstream flow is uniform and subcritical in each case with $\eta^{(1)} = 0.0$ and $B^{(1)} = 0.0$. (a): $b_{\max} = 4.0$, $\Delta = -3.0$. (b): $b_{\max} = 0.4$, $\Delta = -0.3$. (c): $b_{\max} = 0.8$, $\Delta = -0.3$. (d): $b_{\max} = 0.8$, $\Delta = -0.31$ with identical obstacles centered at $x = 60$ and $x = 660$. The steady solutions in (a), (b), and (c) correspond roughly to C_1, C_2, and C_3 in Fig. 7.

it can be expected that a time-dependent adjustment takes place during which the upstream flow (here determined by $B^{(1)}$ and Δ) is altered a sufficient amount to allow a bounded solution. This is essentially the "control" mechanism which is exercised in long-wave flows. In hydraulics, for example, it is well-known (Pratt, 1983b) that the adjustment proceeds according to certain minimal principles which dictate that the upstream flow be altered the smallest amount necessary for a bounded solution to be established. (Thus the hydraulically controlled state contains the minimum upstream energy necessary to surmount the obstacle.) Should such minimal principles also hold for solutions to (28) and (29), the partial solitary wave will be a preferred solution. This follows from the fact (evident upon inspection of Fig. 7a) that, of all the bounded solutions, the solitary wave is the "outermost."

It becomes apparent from the above remarks that the partial solitary wave should be a more common solution than might be expectetd on the basis of steady-state considerations. That this solution should occur in the lee of the second obstacle and not the first apparently follows from the marginally stable character of the solitary wave trajectory; should the partial solitary wave occur in the lee of the first obstacle, the perturbing influence of the second would likely cause the downstream flow to blow up. It is also apparent that $B^{(1)}$ and Δ are controlled by the *second* obstacle and not the first, even if their heights are identical. This follows from the fact that the topography of the first obstacle can be changed a small amount without necessitating changes in the upstream flow.

The theory described above depends upon the flow being "nearly critical." In the laboratory experiments, however, the nearly critical flows are the most difficult to measure owing to the large wavelengths which occur when Fd approaches unity. This experimental finding, while troublesome, can be shown to be at least consistent with the theory. Consider the cnoidal wave solutions to (28) and (29) over a flat bottom of elevation $\tilde{b}^{(2)}$. These solutions surround the equilibrium point $(\eta_+^{(1)}, 0)$ in phase space. The lengths of the waves can be estimated by writing (27) as

$$d^2\eta^{(1)}/dx^2 = -(\eta^{(1)} - \eta_+^{(1)})(\eta^{(1)} - \eta_-^{(1)}), \qquad (35)$$

with $\eta_\pm^{(1)}$ given by (30). If waves of small amplitude $\eta^{(1)} = \eta_+^{(1)} + \hat{\eta}^{(1)}$, with $|\hat{\eta}^{(1)}| \ll \eta_+^{(1)} - \eta_-^{(1)}$ are now considered, (35) can be put in the linear form

$$d^2\hat{\eta}^{(1)}/dx^2 + (\eta_+^{(1)} - \eta_-^{(1)})\hat{\eta}^{(1)} = O(\hat{\eta}^{(1)2}). \qquad (36)$$

The wavelength of periodic solutions is thus $2\pi(\eta_+^{(1)} - \eta_-^{(1)})^{-1/2}$, which grows without bound as the critical state $\eta_+^{(1)} = \eta_-^{(1)}$ is reached [cf. Eq. (33)]. Thus, the small-amplitude waves of the system lengthen without bound as Fd $\rightarrow$ 1.

As a cautionary note, it should be mentioned that the terms "supercritical" and 'subcritical" must be applied with some care when the $O(\delta^2)$ uniform flows are being described. The terms have been used here to indicate the value of the Froude number relative to unity that would be measured in the laboratory, with no implications concerning the ability of disturbances to propagate upstream against the flow.

Finally, note that there is no exclusive relationship between the obstacle heights Δ, and $B^{(1)}$. Unlike long-wave theory, the obstacle shape now becomes important as well.

6. Discussion

The remarks concerning the establishment of the solution of Fig. 8d are intended as intuitive implications

of the experimental results and not as formal proofs. The steady equations (28) and (29) are embedded in a time-dependent equation, and verification of the minimal principles of control would require integration of the more general equation. Such an exercise would undoubtedly prove interesting, because the exact means of upstream control by the topography would be revealed.

One might inquire about the failure of the numerics to give a meaningful solution. Presumably, the failure occurs during the second stage of adjustment (Figs. 2b and c) when the long-wave equations indicate formation of a shock wave between the two obstacles. In reality this shock is probably suppressed by dispersion, leading to the wavelike flow found experimentally. The numerical result emphasizes the importance of accurate specification of the lower boundary condition, a feature commonly lacking in numerical models of atmospheric flow over mountains. If the obstacle in Fig. 2 is "smoothed" to the point of having a single sill, a steady asymptotic state is obtained (Houghton and Kasahara, 1968).

As mentioned in the Introduction, other long-wave theories predict the same instability seen in the present problem. The effects of dispersion are likely similar to those found here, since the nonlinear dispersive equations found to govern nearly-critical states are often of the form (28) and (29). One example, that of a nearly critical rotating-channel flow over topography, has been worked out by Pratt (1984).

Acknowledgments. This work was supported by the Office of Naval Research under Contract N00014-81-C-0062. The author wishes to thank Robert Frazel for valuable assistance in the laboratory, Lore Allen and Beverly Koly for help in preparing the manuscript, and Douglas Mook for a useful suggestion.

REFERENCES

Benjamin, T. B., and M. J. Lighthill, 1954: On cnoidal waves and bores. *Proc. Roy. Soc. London,* **A224,** 448–460.

Booker, J. R., and F. P. Bretherton, 1967: The critical layer for gravity waves in a shear flow. *J. Fluid Mech.,* **27,** 513–539.

Gill, A. E., 1977: The hydraulics of rotating-channel flow. *J. Fluid Mech.,* **80,** 641–671.

——, and E. H. Schumann, 1979: Topographically induced changes in the structure of a coastal inertial jet: Applications to the Agulhas Current. *J. Phys. Oceanogr.,* **9,** 975–991.

Houghton, D. D., and A. Kasahara, 1968: Nonlinear shallow fluid flow over an isolated ridge. *Commun. Pure Appl. Math.,* **21,** 1–23.

Ippen, A. T., and D. R. F. Harleman, 1956: Verification of theory for oblique standing waves. *Trans. ASCE,* **121,** 678–694.

Keller, J. B., 1948: The solitary wave and periodic waves in shallow water. *Commun. Pure Appl. Math.,* **1,** 323–339.

Lax, P., and B. Wendroff, 1960: Systems of conservation laws. *Commun. Pure Appl. Math.,* **13,** 217–237.

Long, R. R., 1954: Some aspects of the flow of stratified fluids II. Experiments with a two-fluid system. *Tellus,* **5,** 42–58.

Pratt, L. J., 1983a: A note on nonlinear flow over obstacles. *Geophys. Astrophys. Fluid Dyn.,* **24,** 63–68.

——, 1983b: On inertial flow over topography. Part I. Semigeostrophic adjustment to an obstacle. *J. Fluid Mech.,* **131,** 195–218.

——, 1984: On inertial flow over topography. Part II. Rotating-channel flow near the critical speed. *J. Fluid Mech.* (in press).

Roed, L. P., 1980: Curvature effects on hydraulically driven inertial boundary currents. *J. Fluid Mech.,* **96,** 395–412.

Whitehead, J. A., A. Leetmaa and R. A. Knox, 1974: Rotating hydraulics of strait and sill flows. *Geophys. Fluid Dyn.,* **6,** 101–125.